Core Mass Estimates in Strong Lensing Galaxy Clusters: A Comparison between Masses Obtained from Detailed Lens Models, Single-halo Lens Models, and Einstein Radii

J. D. Remolina González[1] , K. Sharon[1] , G. Mahler[1,2,3] , C. Fox[1] , C. A. Garcia Diaz[4], K. Napier[1] , L. E. Bleem[5,6] , M. D. Gladders[6,7] , N. Li[8,9] , and A. Niemiec[1,2,3]

[1] Department of Astronomy, University of Michigan, 1085 S. University Ave., Ann Arbor, MI 48109, USA; jremolin@umich.edu
[2] Centre for Extragalactic Astronomy, Department of Physics, Durham University, Durham DH1 3LE, UK
[3] Institute for Computational Cosmology, Durham University, South Road, Durham DH1 3LE, UK
[4] Division of Physics, Engineering, Mathematics, and Computer Science, Delaware State University, 1200 N. Dupont Hwy., Dover, DE, USA
[5] Argonne National Laboratory, High-Energy Physics Division, Argonne, IL 60439, USA
[6] Kavli Institute for Cosmological Physics, University of Chicago, 5640 S. Ellis Ave. Chicago, IL 60637, USA
[7] Department of Astronomy and Astrophysics, University of Chicago, 5640 S. Ellis Ave., Chicago, IL 60637, USA
[8] CAS, Key Laboratory of Space Astronomy and Technology, National Astronomical Observatories, A20 Datun Road, Chaoyang District, Beijing 100012, People's Republic of China
[9] School of Physics and Astronomy, Nottingham University, University Park, Nottingham NG7 2RD, UK
Received 2021 April 8; revised 2021 July 20; accepted 2021 July 20; published 2021 October 20

Abstract

The core mass of galaxy clusters is both an important anchor of the radial mass distribution profile and a probe of structure formation. With thousands of strong lensing galaxy clusters being discovered by current and upcoming surveys, timely, efficient, and accurate core mass estimates are needed. We assess the results of two efficient methods to estimate the core mass of strong lensing clusters: the mass enclosed by the Einstein radius ($M(<\theta_E)$, where θ_E is approximated from arc positions, and a single-halo lens model (M_{SHM}), compared with measurements from publicly available detailed lens models (M_{DLM}) of the same clusters. We use data from the Sloan Giant Arc Survey, the Reionization Lensing Cluster Survey, the *Hubble* Frontier Fields, and the Cluster Lensing and Supernova Survey with *Hubble*. We find a scatter of 18.1% (8.2%) with a bias of -7.1% (1.0%) between $M_{corr}(<\theta_{arcs})$ (M_{SHM}) and M_{DLM}. Last, we compare the statistical uncertainties measured in this work to those from simulations. This work demonstrates the successful application of these methods to observational data. As the effort to efficiently model the mass distribution of strong lensing galaxy clusters continues, we need fast, reliable methods to advance the field.

Unified Astronomy Thesaurus concepts: Galaxy clusters (584); Strong gravitational lensing (1643)

1. Introduction

Galaxy clusters are harbored at the knots of the cosmic web and trace the large-scale structure of the universe, making them ideal cosmic laboratories (see reviews by Allen et al. 2011 and Mantz et al. 2014). The galaxy cluster mass function connects the underlying cosmology and observational properties of galaxy clusters (e.g., Evrard et al. 2002; Pratt et al. 2019; Bocquet et al. 2020). Additional predictions from cosmological simulations include the radial mass distribution of dark matter halos (e.g., Duffy et al. 2008; Meneghetti et al. 2014; Child et al. 2018), which can be directly tested against observations via the concentration measurement (e.g., Oguri et al. 2012; Merten et al. 2015). An accurate account of the cluster mass distribution requires mass estimates that are sensitive at the cores and the outskirts of the galaxy cluster. Crucial to all cluster-based cosmological studies are the sample size, selection function, and good understanding of the systematic uncertainties of the mass estimates coming from observed astrophysical properties (e.g., Evrard et al. 2002; Khedekar & Majumdar 2013; Huterer & Shafer 2018; Bocquet et al. 2019).

One of the methods to measure the total (dark and baryonic) mass distribution of galaxy clusters is using gravitational lensing. Weak lensing (WL) measures the cluster mass at large clustercentric radii, while strong lensing (SL) has the highest resolution at the core of the cluster where the SL evidence is present. The combination of the core mass estimates from SL and outskirts mass estimates from WL or other large-scale mass

proxies can constrain the mass distribution profile of a galaxy cluster and measure its concentration (e.g., Meneghetti et al. 2010; Gralla et al. 2011; Oguri et al. 2012; Merten et al. 2015). Comparisons between the predicted and observed properties of SL galaxy cluster mass distribution have reported possible tension (e.g., Broadhurst & Barkana 2008; Gonzalez et al. 2012; Meneghetti et al. 2013; Killedar et al. 2018); however, these studies have been limited by a complicated selection function and small sample sizes.

Current and upcoming large surveys will discover thousands of SL clusters out to $z \sim 2$ using methods that span the wavelength spectrum. Some of these surveys include the South Pole Telescope (SPT-3G, Benson et al. 2014; SPT-SZ 2500 deg^2, Bleem et al. 2015), Vera Rubin Observatory Legacy Survey of Space and Time (LSST Science Collaboration et al. 2017), and eROSITA (Pillepich et al. 2018). These large samples will require a method to timely, effectively, and accurately measure the core mass of SL clusters.

The SL-based mass measurements are typically based on detailed SL models (e.g., Kneib & Natarajan 2011). Detailed lens models (DLMs) for galaxy clusters with rich SL evidence, such as the Frontier Fields clusters (Lotz et al. 2017), but also less extraordinary clusters, allow for the high degree of complexity required to study substructure in the mass distribution of the cluster (e.g., Ebeling et al. 2017; Mahler et al. 2018; Richard et al. 2021). They necessitate extensive follow-up observations, computational resources, and multiple statistical assessments for the best model selection. However,

more typical SL clusters have a small number of SL constraints, which limits the utility of DLMs (e.g., Smith et al. 2005; Sharon et al. 2020).

The large sample sizes of SL clusters being discovered call for efficient methods to estimate the mass at the core of galaxy clusters. Remolina González et al. (2020, 2021) evaluated two methods for efficiently estimating the mass within the core of SL clusters using the Outer Rim cosmological simulation. Remolina González et al. (2020) evaluated the mass estimate derived from the equation of the Einstein radius of a circularly symmetric lens, and Remolina González et al. (2021) assessed results from simplified single-halo lens models (SHMs). The characterization of the uncertainty and bias of these methods established them as efficient and accurate galaxy cluster core mass estimators for application to large samples of SL galaxy clusters. The two simulation-calibrated methods take orders of magnitude less time and human intervention than DLMs.

The goal of this paper is to test, in real observed clusters, how well these first- and second-order estimates of the core mass compare to DLMs. This paper is organized as follows. In Section 2, we introduce the four SL cluster samples used in our paper and describe our selection of the DLMs. In Section 3, we briefly describe the publicly available lensing algorithms used to compute the DLMs and summarize the SHMs and Einstein radius methods used as efficient estimates of the mass at the core of the galaxy clusters. In Section 4, we describe the SL constraints and selection of the brightest cluster galaxy (BCG); estimate an approximation of the Einstein radius ($\theta_{\rm arcs}$) from the observed lensing constraints; compute the empirically corrected enclosed mass using the Einstein radius equation, $M_{\rm corr}(<\theta_{\rm arcs})$; and compute the aperture mass measured utilizing the SHMs that passed a quick visual inspection, $M_{\rm SHM}$. In Section 5, we measure the scatter and bias of $M_{\rm corr}(<\theta_{\rm arcs})$ and $M_{\rm SHM}$ compared to the mass enclosed by the same aperture in the DLM ($M_{\rm DLM}$) and explore any possible difference due to the variety of lensing algorithms utilized to compute the DLMs. Finally, in Section 6, we present our conclusions and summarize the application of efficient methods to measure the core masses of galaxy clusters.

In our analysis, we adopt a flat ΛCDM cosmology: $\Omega_\Lambda = 0.7$, $\Omega_M = 0.3$, and $H_0 = 70$ km s^{-1} Mpc^{-1}. The large-scale masses are reported in terms of $M_{\Delta \, c}$, defined as the mass enclosed within a radius at which the average density is Δ times the critical density of the universe at the cluster redshift.

2. Observational Data

For this work, we use the data from four well-established SL surveys of clusters with different selection functions. First, we use the Sloan Giant Arcs Survey (SGAS[10]; Hennawi et al. 2008; Sharon et al. 2020), which identified highly magnified lensed galaxies in the Sloan Digital Sky Survey (SDSS; Abazajian et al. 2009; Blanton et al. 2017). Second, we use the Cluster Lensing and Supernova Survey with *Hubble* (CLASH[11]; Postman et al. 2012), designed to study the dark matter distribution in galaxy clusters, perform supernova searches, and detect and characterize high-redshift lensed galaxy clusters. Third, we use the *Hubble* Frontier Fields (HFF[12]) clusters (Lotz et al. 2017), which are some of the best
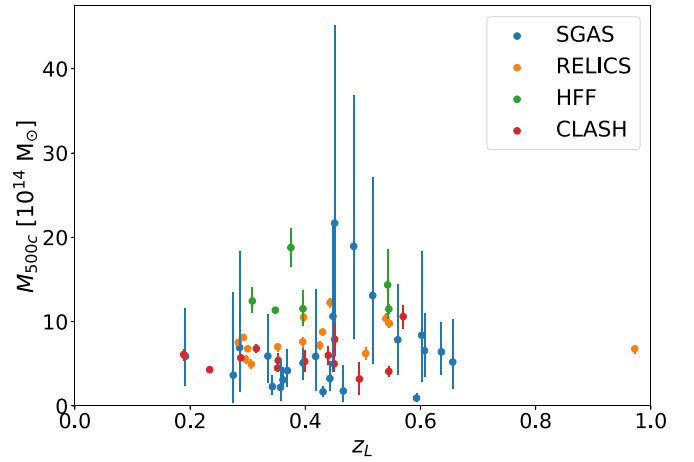

Figure 1. Redshift–mass ($z_{\rm L}$–M_{500c}) distribution of the SL galaxy clusters used in our analysis.

SL clusters, taking advantage of deep imaging and extensive spectroscopic follow-up. Fourth, we use the Reionization Lensing Cluster Survey (RELICS[13]; Coe et al. 2019), designed primarily to find high-redshift ($z \sim 6$–8) lensed galaxy candidates. All four samples base their lensing analyses on multiband *Hubble* Space Telescope (HST) imaging. From these samples of lensing galaxy clusters, we only include clusters with spectroscopically confirmed multiply imaged lensed galaxies. Figure 1 shows the redshift–mass distribution of the galaxy clusters used in our analysis. The large-scale masses, M_{500c}, are taken from Merten et al. (2015), Fox et al. (2021), and references therein.

2.1. SGAS

Galaxy clusters were selected for SGAS from the SDSS Data Release 7 (Abazajian et al. 2009) using the cluster red-sequence algorithm by Gladders & Yee (2000). Color images were created from imaging data in *g*, *r*, *i*, and *z* centered on the detected cluster. The images were visually inspected and scored according to the evidence of strong gravitational lensing. There has been extensive ground- and space-based imaging leading to a multiwavelength picture of these clusters (e.g., 107 HST orbits of the SGAS-HST, GO 13003, PI: Gladders; Sharon et al. 2020). Spectroscopic follow-up of all primary SL arcs is complete, and additional follow-up campaigns obtained redshifts of secondary arcs to improve the fidelity of the lens models (e.g., Bayliss et al. 2011b; Johnson et al. 2017; Sharon et al. 2020, and references therein). Several high-impact targets out of this sample of highly magnified arcs have been studied in detail (e.g., Koester et al. 2010; Bayliss et al. 2014; Sharon et al. 2017; Rigby et al. 2018).

The SGAS clusters are unique due to the selection function employed to create the sample, as they were selected uniquely based on the identification of bright SL features. This led to including some clusters with lower masses when compared to the other three samples of galaxy clusters. Sharon et al. (2020) published and released to the community DLMs for the 37 SGAS clusters observed as part of HST-GO 13003. Out of these 37 galaxy clusters with publicly available lens models (Sharon et al. 2020), we only use 31 in this work. Three clusters (SDSS J0004−0103, SDSS J1002+2031, and

---

[10] https://archive.stsci.edu/pub/hlsp/sgas/
[11] https://www.stsci.edu/postman/CLASH/index.html
[12] https://outerspace.stsci.edu/display/HPR/HST+Frontier+Fields

[13] https://relics.stsci.edu/index.html

Table 1
SL Galaxy Clusters

Galaxy Cluster	z_L	R.A. (J2000)	Decl. (J2000)	DLMs	$N(z_S)$	Arcs/Model Reference
SGAS						
SDSS J0108+0624	0.548	17.17511	6.41210	L	1	a, b
SDSS J0146−0929	0.447	26.73336	−9.49792	L	2	a, c
SDSS J0150+2725	0.306	27.50355	27.42676	L	1	a
SDSS J0333−0651	0.573	53.26940	−6.85635	L	1	a
SDSS J0851+3331	0.369	132.91194	33.51837	L	3	a, d
SDSS J0915+3826	0.396	138.91280	38.44952	L	2	a, d, e
SDSS J0928+2031	0.192	142.01889	20.52919	L	2	a
SDSS J0952+3434	0.357	148.16761	34.57947	L	1	a, f
SDSS J0957+0509	0.448	149.41330	5.15885	L	1	a, d
SDSS J1038+4849	0.431	159.68159	48.82159	L	3	a, d
SDSS J1050+0017	0.593	162.66637	0.28522	L	3	a, g
SDSS J1055+5547	0.466	163.76917	55.80647	L	2	a, d
SDSS J1110+6459	0.656	167.57386	64.99664	L	1	a, c, h
SDSS J1115+1645	0.537	168.76845	16.76058	L	2	a, c, i
SDSS J1138+2754	0.451	174.53731	27.90854	L	2	a, d
SDSS J1152+0930	0.517	178.19748	9.50409	L	1	a
SDSS J1152+3313	0.361	178.00077	33.22827	L	2	a, d
SDSS J1207+5254	0.275	181.89965	52.91644	L	1	a, f
SDSS J1209+2640	0.561	182.34877	26.67950	L	2	a, d, j
SDSS J1329+2243	0.443	202.39391	22.72106	L	1	a, g
SDSS J1336−0331	0.176	204.00035	−3.52496	L	2	a
SDSS J1343+4155	0.418	205.88685	41.91763	L	1	a, d, k
SDSS J1420+3955	0.607	215.16680	39.91859	L	2	a, d
SDSS J1439+1208	0.427	219.79076	12.14043	L	2	a
SDSS J1456+5702	0.484	224.00368	57.03898	L	1	a
SDSS J1522+2535	0.602	230.71985	25.59097	L	1	a
SDSS J1531+3414	0.335	232.79429	34.24031	L	2	a, d
SDSS J1604+2244	0.286	241.04227	22.73858	L	1	a
SDSS J1621+0607	0.343	245.38494	6.12197	L	2	a, d
SDSS J1723+3411	0.442	260.90068	34.19948	L	2	a, f
SDSS J2111−0114	0.636	317.83062	−1.23984	L	1	a, d
CLASH						
Abell 383	0.189	42.01409	−3.52938	LTM.v2, NFW.v2	4	l, n, s, t, u
Abell 611	0.288	120.23673	36.05656	LTM.v2, NFW.v2	2	l, v
MACS J0329.7−0211	0.450	52.42321	−2.19623	L.v1, LTM.v2, NFW.v2	7	l, m, n
MACS J0416.1−2403	0.396	64.03808	−24.06750	See HFF	37	See HFF
MACS J0429.6−0253	0.399	67.40003	−2.88521	L.v1, LTM.v2, NFW.v2	2	l, m
MACS J0717.5+3745	0.545	109.39855	37.75479	See HFF	8	See HFF
MACS J1115.9+0129	0.353	168.96628	1.49861	L.v1, LTM.v2, NFW.v2	2	l, m, n
MACS J1149.5+2223	0.543	177.39875	22.39853	See HFF	7	See HFF
MACS J1206.2−0847	0.440	181.55064	−8.80094	LTM.v2, NFW.v2	4	l, n, w, x
MACS J1311.0−0310	0.494	197.75751	−3.17770	L.v1, LTM.v2, NFW.v2	1	l, m
MACS J1423.8+2404	0.545	215.94949	24.07846	LTM.v2, NFW.v2	2	l, y
MACS J1931.8−2635	0.352	292.95684	−26.57587	L.v1, LTM.v2, NFW.v2	7	l, m
MACS J2129.7−0741	0.570	322.35879	−7.69105	L.v1, LTM.v2, NFW.v2	11	l, m, o
MS J2137−2353	0.315	325.06316	−23.66114	LTM.v2, NFW.v2	2	l
RXC J1347.5−1145	0.451	206.88261	−11.75318	L.v1, LTM.v2, NFW.v2	4	l, m, n, p, q, r
RXC J2129.7+0005	0.234	322.41649	0.08922	L.v1, LTM.v2, NFW.v2	7	l, m
RXC J2248.7−4431	0.348	342.18321	−44.53089	See HFF (Abell S1063)	18	See HFF (Abell S1063)
HFF						
Abell 2744	0.308	3.58626	−30.40017	C.v4, C.v4.1, D.v4 D.v4.1, G.v4, K.v4 S.v4c, W.v4	26	z, aa, ag, ah, ak, al, am
Abell 370	0.375	39.97133	−1.58224	B.v4, B.v4.1, C.v4 D.v4, D.v4.1, G.v4 K.v4, S.v4, W.v4 W.v4.1	32	z, ag, ai, aj, al, am
Abell S1063	0.348	342.18321	−44.53089	C.v4, C.v4.1, D.v4 D.v4.1, G.v4, K.v4	18	z, ab, af, ag, al, am

Table 1
(Continued)

Galaxy Cluster	z_L	R.A. (J2000)	Decl. (J2000)	DLMs	$N(z_S)$	Arcs/Model Reference
MACS J0416.1−2403	0.396	64.03808	−24.06750	S.v4, W.v4, W.v4.1 Cam.v4, C.v4, C.v4.1 D.v4, D.v4.1, G.v4 K.v4, S.v4c, W.v4	37	z, ae, ag, al, am
MACS J0717.5+3745	0.545	109.39855	37.75479	C.v4, C.v4.1, D.v4 D.v4.1, K.v4, S.v4c W.v4, W.v4.1	8	z, ad, al, am
MACS J1149.5+2223	0.543	177.39875	22.39853	C.v4, C.v4.1, D.v4 D.v4.1, K.v4, S.v4c W.v4	7	z, ac, al, am

RELICS

Galaxy Cluster	z_L	R.A. (J2000)	Decl. (J2000)	DLMs	$N(z_S)$	Arcs/Model Reference
Abell 2537	0.297	347.09256	−2.19212	L.v1, G.v2	1	an
Abell 2813	0.292	10.85271	−20.62822	L.v1	1	au
Abell 3192	0.425	59.72531	−29.92527	L.v1	2	ao
Abell S295	0.300	41.35339	−53.02932	LTM.v2	1	ap
CL J0152.7−1357	0.833	28.18242	−13.95515	L.v1, LTM.v1, G.v2	1	aq
MACS J0025.4−1222	0.586	6.36415	−12.37303	LTM.v1	1	ap
MACS J0035.4−2015	0.352	8.85889	−20.26229	L.v1, G.v2	2	au
MACS J0257.1−2325	0.505	44.28647	−23.43468	L.v1, G.v2	1	au
MACS J0417.5−1154	0.443	64.39454	−11.90885	L.v2, G.v3	2	ar
MACS J0553.4−3342	0.430	88.33069	−33.70754	L.v1, G.v2	1	au
MS 1008.1−1224	0.306	152.63455	−12.66469	L.v1	2	au
PLCK G004.5−19.5	0.540	289.27098	−33.52236	L.v1	5	au
RXC J0018.5+1626	0.546	4.63992	16.43787	L.v1	2	au
RXC J0032.1+1808	0.396	8.03914	18.11561	L.v1, LTM.v2, G.v2	1	as
RXC J0232.2−4420	0.284	38.06804	−44.34669	L.v1	1	au
RXC J2211.7−0350	0.397	332.94137	−3.82895	L.v1, G.v2	1	an
SPT−CL J0615−5746	0.972	93.96543	−57.78011	L.v1, LTM.v1	2	at

Notes. The SL galaxy clusters included in this work. Here z_L is the lens redshift of the galaxy cluster; R.A. and Decl. are the R.A. and decl. of the selected BCG, respectively; and $N(z_S)$ is the number of multiply imaged lensed background sources with spectroscopic redshifts that are used in this paper. The DLMs column indicates the names of the lens modeling teams or algorithms and the versions that are utilized for the comparison in this work. A brief description of the samples can be found in Section 2: SGAS (see Section 2.1), CLASH (see Section 2.2), HFF (see Section 2.3), and RELICS (see Section 2.4).
DLMs used in this work (see also Section 2):
SGAS: L = Lenstool
CLASH: L = Lenstool; LTM = Light-Traces-Mass; NFW = LTM + eNFW; .v1 = version 1; .v2 = version 2
HFF: B = Bradač (SWUnited); C = CATS (Lenstool); Cam = Caminha (Lenstool); D = Diego (WSLAP+); G = Glafic (GLAFIC); K = Keeton (GRAVLENS); S = Sharon (Lenstool); W = Williams (GRALE); .v4 = version 4; .v4c = version 4 corrected; .v4.1 = version 4.1
RELICS: G = GLAFIC; L = Lenstool; LTM = Light-Traces-Mass; .v1 = version 1; .v2 = version 2; .v3 = version 3
References: (a) Sharon et al. (2020); (b) Rigby et al. (2018); (c) Stark et al. (2013); (d) Bayliss et al. (2011a); (e) Bayliss et al. (2010); (f) Kubo et al. (2010); (g) Bayliss et al. (2014); (h) Johnson et al. (2017): (i) Bayliss (2012); (j) Ofek et al. (2008); (k) Diehl et al. (2009); (l) Zitrin et al. (2015); (m) Caminha et al. (2019); (n) CLASH-VLT Rosati et al. (in preparation); (o) Huang et al. (2016); (p) Ravindranath & Ho (2002); (q) Bradač et al. (2008); (r) Halkola et al. (2008); (s) Smith et al. (2001); (t) Newman et al. (2011); (u) Richard et al. (2011); (v) Newman et al. (2013); (w) Ebeling et al. (2009); (x) Zitrin et al. (2012); (y) Limousin et al. (2010); (z) Johnson et al. (2014); (aa) Zitrin et al. (2014); (ab) Diego et al. (2016); (ac) Jauzac et al. (2016); (ad) Limousin et al. (2016); (ae) Caminha et al. (2017); (af) Karman et al. (2017); (ag) Kawamata et al. (2018); (ah) Mahler et al. (2018); (ai) Strait et al. (2018); (aj) Lagattuta et al. (2019); (ak) Sebesta et al. (2019); (al) Vega-Ferrero et al. (2019); (am) Raney et al. (2020a); (an) Cerny et al. (2018); (ao) Hsu et al. (2013); (ap) Cibirka et al. (2018); (aq) Acebron et al. (2019); (ar) Mahler et al. (2019); (as) Acebron et al. (2020); (at) Paterno-Mahler et al. (2018); (au) RELICS public data release (see Section 2.4).

SDSS J1527+0652) are not included due to being poorly constrained (given a classification of C or lower; see Sharon et al. 2020 for more details). Two galaxy clusters (SDSS J1156 +1911 and SDSS J1632+3500) lack any spectroscopically confirmed multiply imaged sources. One galaxy cluster (SDSS J2243−0935) has one spectroscopically confirmed flat giant arc located between two cluster cores, making it unsuitable for the methods used here. In Table 1, the list of the SGAS clusters is shown with their corresponding redshift, the R.A. and decl. of the selected BCG, and the number of strongly lensed background sources with spectroscopic redshifts that are used as lens modeling constraints.

2.2. CLASH

The CLASH (Postman et al. 2012) multicycle treasury project observed 25 galaxy clusters for a total of 525 HST orbits over a period of nearly 3 yr utilizing 16 HST filters. The main science goals included studying the matter distribution of galaxy clusters, particularly the mass concentration (e.g., Merten et al. 2015); detecting supernovae (e.g., Graur et al. 2014); and detecting and characterizing high-redshift galaxies magnified by the galaxy cluster (e.g., Coe et al. 2013). Of the 25 galaxy clusters, 20 are X-ray-selected, dynamically relaxed (determined from their circularly symmetric X-ray surface brightness distribution), and massive clusters (X-ray temperatures $T_x > 5$ keV). The majority of

these clusters showed SL evidence from ancillary data. The last five galaxy clusters were selected solely for being exceptional strong lenses. Four of the galaxy clusters (Abell S1063, MACS J0416.1 −2403, MACS J0717.5+3745, and MACS J1149.5+2223) were later selected for the HFF (see Section 2.3), and we only utilize the HFF lens models for these clusters. The community follow-up effort has resulted in the identification of many lensing constraints with measured spectroscopic redshifts for the 13 galaxy clusters included in this work. Detailed lensing models by Zitrin et al. (2015) and Caminha et al. (2019) have been made publicly available. In Table 1, we list the CLASH galaxy clusters utilized in our analysis and their corresponding references.

2.3. HFF

The HFF (Lotz et al. 2017) project observed six galaxy clusters and adjacent ("parallel") fields using Director's Discretionary Time, obtaining extremely deep multiband imaging (140 HST orbits per cluster for a total of 840 HST orbits of Director's Discretionary Time) with the primary goal of studying the magnified background universe. The clusters were selected for their observability from space- (*HST*, *Spitzer*, and the *James Webb Space Telescope*) and ground-based observatories, their lensing strength, and the availability of preexisting ancillary data. These galaxy clusters have become some of the most studied galaxy clusters due to the community investment in extensive multi-wavelength imaging and spectroscopic follow-up, resulting in large numbers of SL constraints identified and used in the DLMs (Johnson et al. 2014; Zitrin et al. 2014; Diego et al. 2016; Jauzac et al. 2016; Limousin et al. 2016; Caminha et al. 2017; Karman et al. 2017; Kawamata et al. 2018; Mahler et al. 2018; Strait et al. 2018; Lagattuta et al. 2019; Sebesta et al. 2019; Vega-Ferrero et al. 2019; Raney et al. 2020a; and references therein). The HFF program provides a unique opportunity to study the statistical and systematic uncertainties in the lensing outputs due to the large number of diverse lensing algorithms that have computed DLMs of these clusters (e.g., Meneghetti et al. 2017; Priewe et al. 2017; Remolina González et al. 2018; Raney et al. 2020b all compare different aspects of the HFF lens models using different algorithms). In this work, we include the fourth version of the public lens models, which is the most recent release. The clusters and references for the models are listed in Table 1.

2.4. RELICS

The RELICS program selected 41 galaxy clusters for shallow multiband observation with HST with the primary goal of delivering a large sample of high-redshift ($z \sim 6$–8) galaxies (Salmon et al. 2018, 2020; Mainali et al. 2020; Strait et al. 2020). Twenty-one clusters where selected from a subsample of the most massive Planck clusters (using the Sunyaev-Zel'dovich effect, Sunyaev & Zeldovich 1970, to estimate their mass; Planck Collaboration et al. 2016). The other 20 clusters were selected based on a prior identification as prominent strong lenses in the available imaging data. The reasoning used for this selection is the expectation that the mass of the galaxy cluster relates to its potential to have a large lensing cross section, leading to an increase in the chance to find high-redshift lensed sources.

The selection function employed for assembling the list of RELICS clusters explores the high-mass parameter space. In addition, the wider and shallower imaging observing strategy (total of 188 HST orbits, GO 14096; PI: Coe) is a clear example

of the challenges confronted by lensing surveys where only the primary and some of the secondary arcs are readily identifiable, leading to a limited number of constraints available for the lens modeling analysis (Acebron et al. 2018, 2019, 2020; Cerny et al. 2018; Cibirka et al. 2018; Paterno-Mahler et al. 2018; Mahler et al. 2019, and references therein). Of the 41 galaxy clusters observed, 34 have publicly available DLMs, and only 17 have publicly available spectroscopically confirmed multiple imaged sources. Following Fox et al. (2021), we inspect the unpublished DLMs and include in our analysis only models whose predicted lensed images are within $1\rlap{.}{''}5$ of the observed lensing evidence and do not produce critical curves or masses that are not justified by the lensing constraints. In Table 1, we present the list of the RELICS clusters used in our analysis with their corresponding lens redshift, R.A. and decl. of the selected BCG, and number of background source spectroscopic redshifts that were used to constrain $M_{corr}(<\theta_{arcs})$ and M_{SHM} in this paper.

3. Lens Modeling and Einstein Radius

Strong lens modeling analyses use the positional and redshift measurements of lensed galaxies (arcs) as constraints to model the underlying mass distribution. There are a variety of well-established lensing algorithms that have been used extensively to study both the galaxy cluster and the magnified background universe. Below, we provide a brief description of the lensing algorithms that were employed to compute the publicly available DLMs used in our analysis. We also briefly describe the Einstein radius mass estimate and SHMs, which were recently evaluated by Remolina González et al. (2020) and Remolina González et al. (2021), respectively, as methods to quickly and effectively measure the mass at the core of SL galaxy clusters.

3.1. Detailed Lens Models

Lensing algorithms are usually grouped into three categories: parametric, nonparametric, and hybrid, based on the parameterization of the modeled mass distribution. Parametric models utilize a combination of parametric functions to describe the mass distribution of the lens plane. Nonparametric, or "free-form," algorithms make no assumption on the functional form of the mass distribution. Hybrid models are a combination of these two forms. The degree to which mass is assumed to be correlated with the observed light distribution also varies among the different algorithms.

The parametric models that are used in this work include GLAFIC (Oguri 2010; Ishigaki et al. 2015; Kawamata et al. 2016), GRAVLENS (Keeton 2010; McCully et al. 2014), and Lenstool (Kneib et al. 1996; Jullo et al. 2007; Jullo & Kneib 2009; Niemiec et al. 2020). These algorithms use a variety of analytical mass distributions for both the cluster-scale dark matter halos and the contribution of the galaxy cluster members. Light-Traces-Mass (LTM; Broadhurst et al. 2005; Zitrin et al. 2009, 2015) assigns mass to a parameterized description of the light distribution, and LTM with elliptical Navarro–Frenk–White (NFW) profiles (LTM+eNFW; Zitrin et al. 2009, 2015) combines this approach with analytical mass distributions as the parametric models. The free-form algorithms include Strong and Weak Lensing United (SWUnited; Bradač et al. 2006, 2009), which performs an iterative minimization of a nonregular adaptive grid, and GRALE (Liesenborgs et al. 2006; Mohammed et al. 2014), which uses a genetic algorithm to iteratively refine the mass distribution on a grid. Last, the

hybrid algorithm Weak & Strong Lensing Analysis Package (WSLAP+; Diego et al. 2005, 2007, 2016) is a nonparametric algorithm with the addition of a parameterized distribution for the cluster member contribution. Modeling algorithms also differ by their assumptions of the extent of correlation between light and mass. A variety of techniques are employed to explore the parameter space, determine the model that best reproduces the observed lensing configuration, and determine statistical uncertainties.

The DLMs can be highly complex, adding the flexibility required for detailed studies of galaxy cluster properties, their surrounding environment, uncorrelated structure along the line of sight, the magnified background universe, and cosmology. This high complexity of the models relies on a large number of free parameters requiring a large number of constraints, i.e., multiply imaged lensed galaxies, whose availability becomes a limiting factor in the modeling process. The versatility of DLMs also means the models are not unique and require care in their construction and evaluation; statistical assessments are employed to select between models (e,g., Acebron et al. 2017; Paterno-Mahler et al. 2018; Lagattuta et al. 2019; Mahler et al. 2019). High-fidelity lens models of galaxy clusters with rich SL evidence require extensive follow-up observations, a large investment of computational and human resources, and multiple iterations of the lensing analysis and modeling process to revise the models as new observational evidence becomes available (e.g., Sharon et al. 2012; Johnson et al. 2014; Jauzac et al. 2015).

To determine the statistical uncertainties of the public DLMs used in this work, we use the "range" maps that are provided with them. The range maps are the same lensing products as the best-fit products, except they are derived from sets of parameters that sample the parameter space of each model and provide a handle on how the variation in model parameters affects the lensing-derived projected mass density.

3.2. Single-halo Lens Models

The SHMs computed in this analysis follow Remolina González et al. (2021). We use Lenstool to compute the SHM in one lens plane with a single cluster-scale dark matter halo. The mass distribution is parameterized using a dual pseudoisothermal ellipsoid (dPIE; Elíasdóttir et al. 2007) and no contribution from galaxy cluster members. Of the seven dPIE parameters ($\Delta\alpha$ and $\Delta\delta$ are the R.A. and decl., ϵ is the ellipticity, θ is the position angle, r_{core} is the core radius, r_{cut} is the truncation radius, and σ is the effective velocity dispersion), only six are optimized as we set the truncating radius to a fixed 1500 kpc, as is typically done in DLMs in the literature (note that this projected radius is also similar to the splashback radius; e.g., Umetsu & Diemer 2017; Shin et al. 2019). We use broad priors in the six free parameters of the dPIE potential: $-8\overset{''}{.}0 < \Delta\alpha$, $\Delta\delta < 8\overset{''}{.}0$, $0.0 < \epsilon < 0.9$, $0° < \theta < 180°$, 50 kpc $< r_{core} < 150$ kpc, and 500 km s$^{-1} < \sigma < 1500$ km s^{-1}. The small number of free parameters calls for only a handful of constraints, with a minimum of six constraints required. This can be satisfied with as few as four multiple images of the same source, as each identified set of n multiple images contributes $2n - 2$ constraints. With the image identification in hand (see Section 4.1), the models can be computed quickly and with limited human intervention. Generally, the SHM can be automatically computed once the cluster redshift, center initial

position (e.g., the BCG), and position and redshift of the arcs are measured.

Remolina González et al. (2021) assessed the scatter and bias associated with the mass estimated by this approach by comparing it to the "true" mass from mock SL images based on the Outer Rim (Heitmann et al. 2019) cosmological simulation. They measured the single-halo aperture mass within the effective Einstein radius, M_{SHM}, from the projected mass distribution derived by the SHM and compared it to the mass from the simulated data, which they measured within the same radius. They found an overall scatter of 8.5% with a bias of 0.9% in M_{SHM}. When a quick visual inspection is performed and only the models that pass the inspection are used, the scatter and bias of M_{SHM} improve to 3.3% and 0.3%, respectively. The visual inspection is conducted in order to identify those SHMs that fail to reproduce the observed lensing configuration and predict arcs in regions where no multiple images are found.

The aperture within which the masses were measured in Remolina González et al. (2021), as well as in this work, is the effective Einstein radius (denoted as $e\theta_E$ in Remolina González et al. 2021), defined as the radius of a circle with the same area enclosed by the tangential critical curve of the SHM. The critical curves are derived from the convergence and shear outputs of the best-fit SHM. We use a notation of $e\theta_{E,SHM}$ instead of $e\theta_E$ in order to reduce confusion with other notations used in this paper.

3.3. Einstein Radius

The mass enclosed by the Einstein radius, $M(<\theta_E)$, is a quick method to estimate cluster core mass, where SL is detected:

$$M(<\theta_E) = \Sigma_{cr}(z_L, z_S) \, \pi \, [D_L(z_L)\theta_E]^2, \qquad (1)$$

where $\Sigma_{cr}(z_L, z_S)$ is the critical surface density, $D_L(z_L)$ is the angular diameter distance from the observer to the lens, z_L is the lens redshift, z_S is the background source redshift, and θ_E is the Einstein radius. The main assumption of this method is that the projected mass distribution of the lens is circularly symmetric (Narayan & Bartelmann 1996; Schneider 2006; Kochanek 2006; Bartelmann 2010; Kneib & Natarajan 2011). In this method, a crude estimate of the Einstein radius is obtained from the occurrence of arcs around the center of the lens, e.g., by minimizing the quadrature sum of the difference between the arc positions and the nearest point to them on the circle.

Remolina González et al. (2020) quantified the scatter and bias of the mass enclosed by the Einstein radius method using mock lensed images from the Outer Rim (Heitmann et al. 2019) simulations. They found that the scatter and bias increase with deviation from spherical symmetry and with the estimated θ_E and introduced empirical corrections to debias the results and reduce the scatter.

The empirical correction was calibrated for estimated Einstein radii of $\theta_E \leqslant 30\overset{''}{.}0$ and different centering assumptions. The corrected mass enclosed by the estimated Einstein radius, $M_{corr}(<\theta_E)$, is reported to have no bias and a scatter of 10.9% for the quadratic (12.1% for the linear) corrected masses. Only the identified tangential arcs are used in this method.

We use the same methods as Remolina González et al. (2020) for estimating the Einstein radius and calculating the

enclosed mass using Equation (1). However, in the rest of the paper, we denote the estimated Einstein radius used in this method as θ_{arcs} instead of θ_{E}, to highlight its deviation from the "true" or "effective" Einstein radii of the lens and reduce confusion with other notations used in this paper. The empirically corrected mass estimated by this method is denoted $M_{\mathrm{corr}}(<\theta_{\mathrm{arcs}})$ hereafter.

Following the recommendation and procedures established by Remolina González et al. (2020), when applying this method to the observational data, we use the BCG of the galaxy cluster as our fixed center.

The projected arc radii in this work extend beyond the calibrated range (see left panel of Figure 2). We therefore use caution when applying this method to our sample and investigate different choices in its application at large estimated Einstein radii. We apply the quadratic empirical correction for $\theta_{\mathrm{arcs}} \leqslant 30''.0$, as recommended by Remolina González et al. (2020), and the linear empirical correction for the rest. In addition to the full sample, we report results for a subsample of $\theta_{\mathrm{arcs}} \leqslant 20''.0$, which is better represented by the simulated data used by Remolina González et al. (2020) to calibrate the method.

4. Methodology

In the following section, we describe the input constraints needed to compute $M_{\mathrm{corr}}(<\theta_{\mathrm{arcs}})$ and M_{SHM}. Following the work by Remolina González et al. (2020, 2021), we compute the core mass for the sample of SL galaxy clusters analyzed in this work.

4.1. Arc Catalogs

We use the lensing constraints (arcs) that were identified and listed with the public lens models. For this work, we only use constraints with spectroscopic redshifts (references for the arc catalogs are given in Section 2). We inspect the lensed galaxies and determine if they are tangential or radial arcs depending on the direction of their distortion. Only the tangential arcs are used in the fits for the $M(<\theta_{\mathrm{E}})$ method, but all of the arcs are included when computing the SHMs.

4.2. BCG Selection

The position of the BCG serves as the initial position for the cluster-scale dark matter halo in the SHMs and the fixed center in the Einstein radius mass estimate. The BCGs were selected by their magnitude from a cluster member catalog (see Postman et al. 2012 and Fox et al. 2021) and then confirmed by visual inspection.

4.3. Computing M_{SHM} and $M_{corr}(<\theta_{arcs})$

SHM method—Using the catalog of the arcs and the selected BCG, we compute the SHMs, compute $e\theta_{\mathrm{E,SHM}}$ from the SHM critical curves, and measure the aperture mass within a radius of $e\theta_{\mathrm{E,SHM}}$. As noted in Section 3.2, $e\theta_{\mathrm{E,SHM}}$ is defined as the radius of a circle with the same area as the tangential critical curve. We compute an SHM for each set (also known as "family") of multiply imaged background sources. The resulting SHM outputs (projected mass density, convergence, and shear) are used to compute M_{SHM} as described in Section 3.2.

There are cases where a galaxy cluster has multiple arc families, although none of the individual families satisfy the minimum number of six constraints needed (the total number of constraints for a given model is $\Sigma(2n_i - 2)$, where n_i is the number of constrains for a background source i). We therefore compute one SHM for each cluster that uses all of the families as constraints; thus, the minimum number of constraints needed is attained. For these models, the SHM outputs are computed for a source redshift of $z_{\mathrm{S}} = 2.0$. All of the SHMs are inspected, and only the ones that pass the quick visual inspection are used in our analysis. From a total of 67 clusters, 62 (29 SGAS, 15 RELICS, 6 HFF, and 12 CLASH) have enough constraints to compute an SHM, i.e., six or more constraints. Following the visual inspection, only 54 (23 SGAS, 13 RELICS, 6 HFF, and 12 CLASH) clusters remain in our analysis.

We plot the distribution of effective radii, $e\theta_{\mathrm{E,SHM}}$, measured from the SHMs that pass the visual inspection in the right panel of Figure 2. The distribution of $e\theta_{\mathrm{E,SHM}}$ generally follows the number of clusters in each survey, as most clusters only have one or two independent SHMs that could be computed and pass the visual inspection. We note that while the depth of the HFF data leads to an unprecedented number of strongly lensed galaxies overall, many of the arc families do not have four or more secure multiple images each. We find that SGAS models occupy the lower end of the $e\theta_{\mathrm{E,SHM}}$ distribution, followed by RELICS, CLASH, and HFF. The distributions of effective Einstein radii measured from the SHM emphasize the difference in the selection function of the SL sample, as CLASH, HFF, and RELICS attempted to select clusters with large lensing cross sections, to increase the chances of observing magnified high-redshift galaxies.

Einstein radius method—Utilizing the same catalog of arcs and BCG positions, we geometrically fit each arc family with a circle that minimizes the quadrature sum of the distances between the tangential arc positions and the nearest points to them on the circle, following Remolina González et al. (2020). The resulting radius, θ_{arcs}, is assumed to be an approximation of θ_{E} in Equation (1). We measure at least one θ_{arcs} per galaxy cluster. The measured θ_{arcs} is then used to compute $M_{\mathrm{corr}}(<\theta_{\mathrm{arcs}})$ as described in Section 3.3, using Equation (1) and the empirical correction from Remolina González et al. (2020).

We plot the distribution of all θ_{arcs} in the left panel of Figure 2. Unlike the SHM case, the $M_{\mathrm{corr}}(<\theta_{\mathrm{arcs}})$ can be computed for any number of multiple images of a given lensed source, resulting in an $M_{\mathrm{corr}}(<\theta_{\mathrm{arcs}})$ measurement for each strongly lensed source with spectroscopic redshift. The deep observations and extensive spectroscopic follow-up of the six HFF clusters resulted in a large number of lensed sources with spectroscopic redshifts, which extend to large clustercentric radii. In all of the other fields, where only a few lensed sources per cluster have spectroscopic redshifts, the number of measurements is driven by the number of clusters in each sample, and the identified sources have smaller clustercentric distances.

4.4. Statistics

Depending on the number of arcs and arc families available for each method, each cluster enables up to 37 θ_{arcs} measurements and six SHMs. The measurements in each cluster are expected to be correlated, and their distribution can
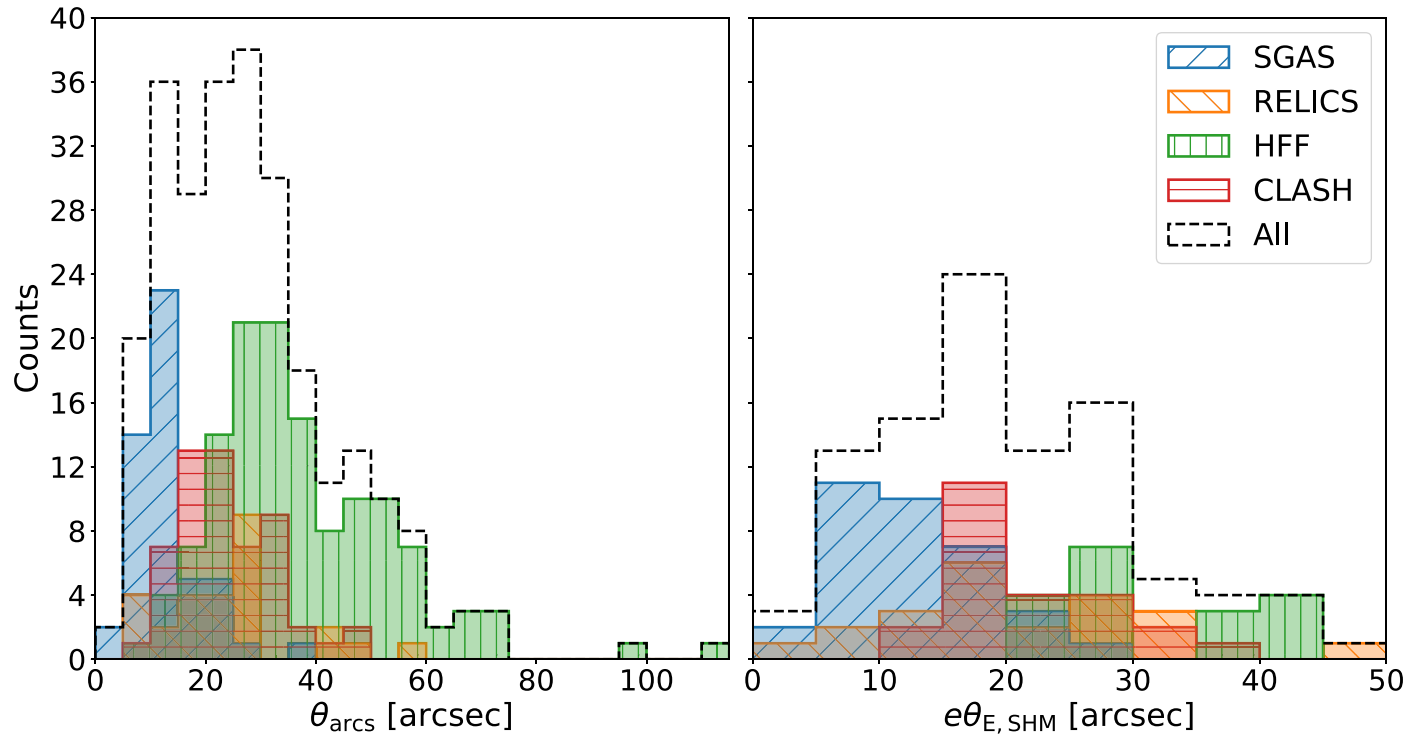
Figure 2. Distribution of θ_{arcs} and $e\theta_{E,SHM}$ as measured from the two different mass estimate methods. The approximate Einstein radius (θ_{arcs}; left panel) is measured from the geometric fit of a circle that minimizes the quadrature sum of distances between the tangential arc positions and the nearest points to them on the circle of a single background source. The SHM-derived effective Einstein radius ($e\theta_{E,SHM}$; right panel) is measured as the radius of a circle with the same area enclosed by the tangential critical curve of the SHMs. This figure shows only results from SHMs that passed the visual inspection. Both θ_{arcs} and $e\theta_{E,SHM}$ have units of arcseconds. The black dashed line represents the total counts, and the colors denote the counts from the four different surveys of SL galaxy clusters. As expected from the selection functions of these samples, the SGAS clusters have lower θ_{arcs} and $e\theta_{E,SHM}$, followed by the RELICS, CLASH, and HFF galaxy clusters. The deep observation and extensive follow-up of the six HFF clusters result in a large number of lensed sources with spectroscopic redshifts extending to large clustercentric radii, which is reflected in the distribution of θ_{arcs}. The SGAS, CLASH (except for those that are also part of HFF), and RELICS have only a few lensed sources per cluster with spectroscopic redshifts and are found at smaller clustercentric distances.
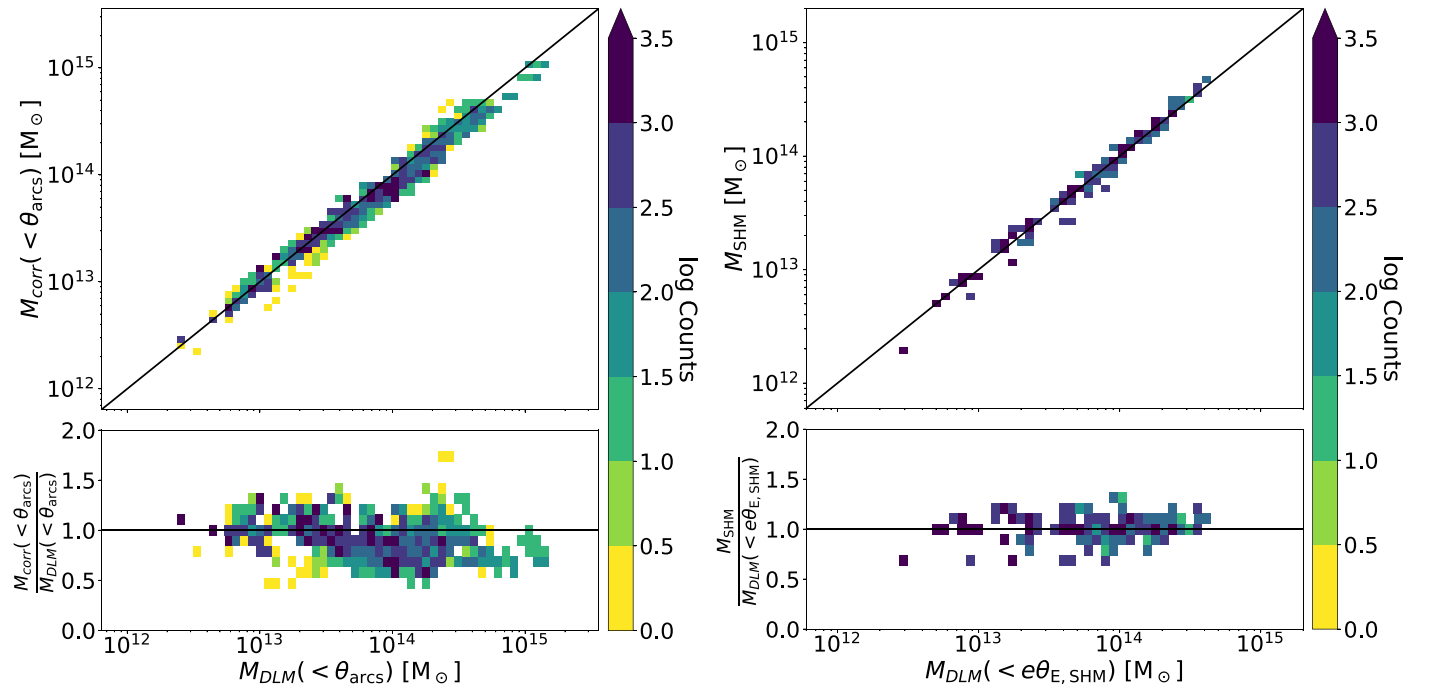
Figure 3. Mass comparison between the efficient mass estimates, $M_{\mathrm{corr}}(<\theta_{\mathrm{arcs}})$ and M_{SHM}, and the DLM, M_{DLM}. The left panels are for the mass enclosed by the approximate Einstein radius, $M_{\mathrm{corr}}(<\theta_{\mathrm{arcs}})$, and the right panels are for the SHM that passed the visual inspection, M_{SHM}. The top panels show the direct comparison between the masses, and the bottom panels are the ratio of the mass measurements. The total numbers of counts are the 62,000 and 52,000 sampled data points for $M_{\mathrm{corr}}(<\theta_{\mathrm{arcs}})$ and M_{SHM}, respectively (see Section 4.4). The black lines indicate the one-to-one line, where $M_{\mathrm{corr}}(<\theta_{\mathrm{arcs}})$ or M_{SHM} equals M_{DLM}. We find that the distribution of $M_{\mathrm{corr}}(<\theta_{\mathrm{arcs}})$ is biased low, particularly at large M_{DLM}, and the distribution of M_{SHM} is biased slightly high.

inform the statistical uncertainty. On the other hand, individual clusters are independent of each other.

We follow Remolina González et al. (2020, 2021) and build a statistical sample for each method ($M(<\theta_{\mathrm{E}})$ and SHM) to take into account multiple mass estimates for a single galaxy cluster and set the statistical weight for each cluster equal to 1.

Depending on the number of available arc families, a given galaxy cluster may have more than one SHM or Einstein radius mass estimate. For the SHM mass estimate, we select at random one M_{SHM} from the available SHMs for each cluster. This process is repeated 1000 times per cluster, leading to a sample of 62,000 points from all SHMs, of which 54,000 M_{SHM} points are ones that passed the quick visual inspection.

A similar process is employed for the Einstein radius mass estimate. For each cluster, we select at random one of its available arc families and select a θ_{arcs} by sampling from a normal distribution centered on the fiducial θ_{arcs} measurement and a standard deviation equal to the uncertainty from the radius fit. We then calculate the relevant mass from Equation (1). Again, we repeat the process 1000 times per cluster, leading to a sample of 67,000 $M_{\mathrm{corr}}(<\theta_{\mathrm{arcs}})$ points.

For comparison of each of these sample points to M_{DLM}, the uncertainty in the DLM mass is accounted for by drawing from a normal distribution centered on the best-fit DLM and with standard deviation computed from the DLM range maps. If a cluster has more than one DLM (see Section 2), one DLM was selected at random for each of the 1000 sampling points.

5. Analysis of Results

In the following section, we compare the galaxy cluster core mass measurements obtained by the quick methods, $M_{\mathrm{corr}}(<\theta_{\mathrm{arcs}})$ and M_{SHM}, to the mass enclosed by the respective mass apertures from the DLMs, M_{DLM}. We evaluate the results

against several properties of the lens system and compare the scatter to that expected from simulations (Remolina González et al. 2020, 2021) and the statistical uncertainty of DLMs. In this work, the scatter is defined as half of the difference between the 84th and 16th percentiles. The bias is determined from the median of the distribution.

5.1. Mass Enclosed by the Estimated Einstein Radius, $\mathrm{M}_{corr}(<\theta_{arcs})$

In left panels of Figure 3, we plot the direct comparison between the corrected mass from the Einstein radius method, $M_{\mathrm{corr}}(<\theta_{\mathrm{arcs}})$, and the mass enclosed by the same aperture from the best-fit DLM, M_{DLM}, for all clusters. We measure an overall scatter of 18.1% and bias of −7.1% in $M_{\mathrm{corr}}(<\theta_{\mathrm{arcs}})$ compared to M_{DLM}. We find that the distribution is biased low, particularly at large M_{DLM} values. The observed negative bias is reduced when excluding systems with a large estimated Einstein radius ($\theta_{\mathrm{arcs}} > 20\overset{''}{.}0$). For the subsample of $\theta_{\mathrm{arcs}} \leqslant 20\overset{''}{.}0$, the scatter is 14.4%, and the bias is −4.3%. This bias could possibly be addressed by extending the work of Remolina González et al. (2020) to larger radii by using simulations that include lower magnification lensed sources at larger clustercentric distances.

5.2. Mass Estimate from SHMs, M_{SHM}

We assess the results of the entire SHM sample and the subsample of models that passed the visual inspection. In the right panels of Figure 3, we plot the direct comparison between the aperture mass of the SHM that passed the visual inspection, M_{SHM}, and the mass enclosed by the same aperture in the best-fit DLM, M_{DLM}. For the entire SHM sample, we measure an overall scatter of 12.4% and a bias of 2.4%. For the SHMs that
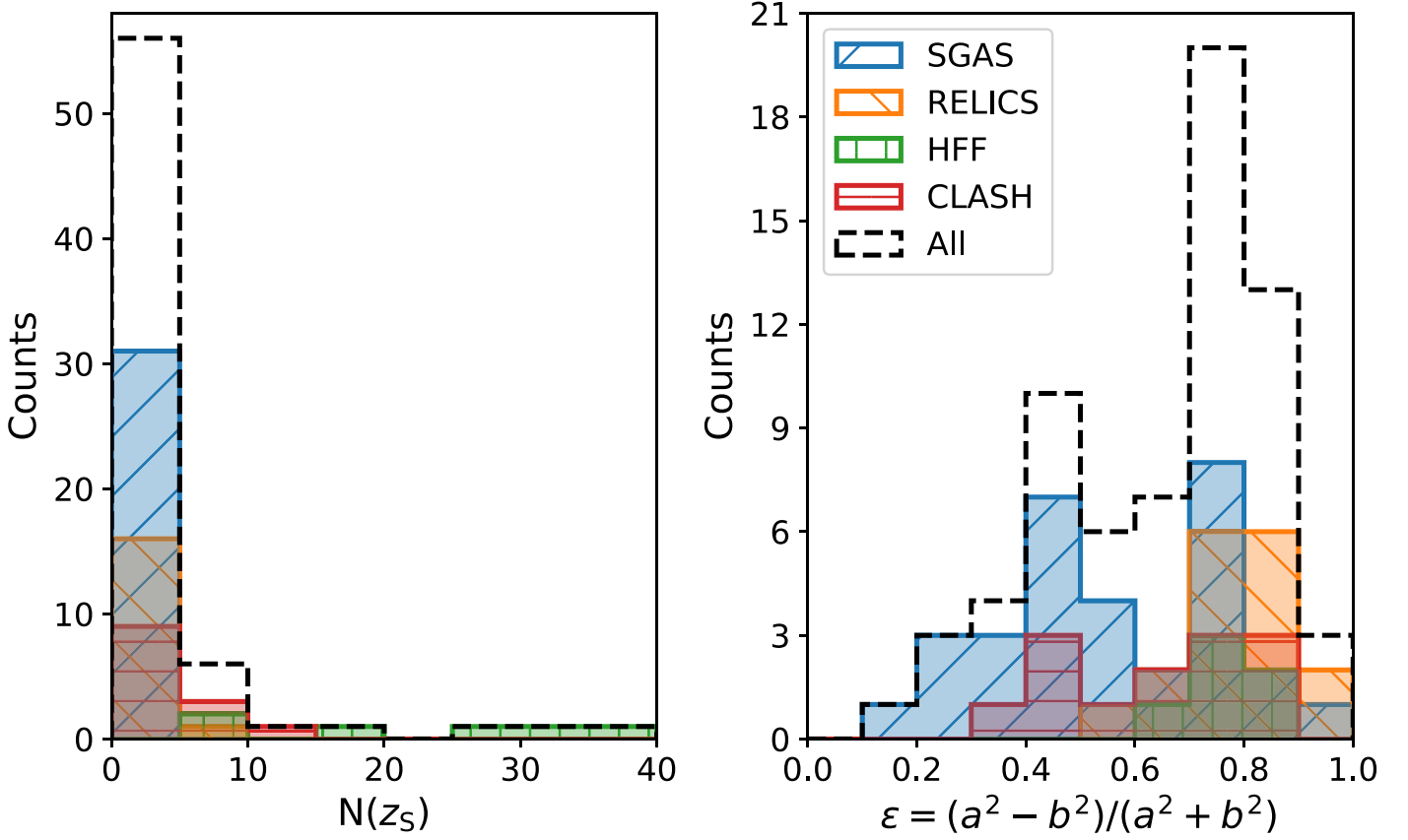
Figure 4. Distribution of the total number of multiply imaged lensed sources with spectroscopic redshifts and galaxy cluster deviation from circular symmetry. The total number of multiply imaged background sources with spectroscopic redshifts per galaxy cluster, $N(z_S)$, is shown in the left panel (see also Table 1). The distribution is indicative of the extensive observational and spectroscopic investment by the community in rich lensing clusters like the HFF. The deviation from circular symmetry is encoded in the ellipticity of the DLM critical curve, $\epsilon = (a^2 - b^2)/(a^2 + b^2)$, where a and b are the semimajor and semiminor axes of an ellipse fit to the tangential critical curve for a source redshift $z_S = 2.0$ computed from best-fit DLMs. When multiple DLMs exist for a galaxy cluster, the median ϵ is used. We find that the distribution matches expectations, with the HFF having well-reported complex and elongated mass distributions. We find that all of the galaxy clusters from HFF and RELICS have $\epsilon > 0.5$, while the CLASH and SGAS clusters are the only samples with some galaxy clusters with $\epsilon < 0.5$.

passed the quick visual inspection, we measure an overall scatter of 8.2% and a bias of 1.0% between M_{SHM} and M_{DLM}. Similar to Remolina González et al. (2021), we find that the visual inspection helps decrease the scatter and bias between M_{SHM} and M_{DLM}.

5.3. Analysis of Systematics

In this subsection, we discuss possible correlations between the scatter in the efficient mass estimates with the aperture radii within which they are measured (θ_{arcs} or $e\theta_{E,SHM}$), the total number of multiply imaged lensed background sources with spectroscopic redshifts available for each lens ($N(z_S)$), and the galaxy cluster deviation from circular symmetry (ϵ). The distributions of these properties in our sample are shown in Figures 2 and 4 and briefly discussed below.

As can be seen in Table 1 and the left panel of Figure 4, most of the clusters in our sample have five or fewer multiply imaged background sources with spectroscopic redshifts, with the HFF and CLASH samples dominating the high-$N(z_S)$ end. The distribution of $N(z_S)$ is indicative of and stems from the extensive observational and spectroscopic efforts by the community in these fields. Clusters with $N(z_S) > 5$ are shown to have highly accurate DLMs (Johnson & Sharon 2016)

and enable DLMs with sufficient flexibility to describe complex mass distributions. We therefore compare clusters that fall within three broad bins: $N(z_S) = 1$, $2 \leqslant N(z_S) \leqslant 5$, and $N(z_S) \geqslant 6$.

The deviation from circular symmetry of each cluster lens is estimated from their best-fit DLM. We compute the tangential critical curve for a background source redshift of $z_S = 2.0$ and fit an ellipse using the technique described in Fitzgibbon et al. (1996). The resultant ellipticity adopts the following form: $\epsilon = (a^2 - b^2)/(a^2 + b^2)$, where a and b are the semimajor and semiminor axes of the fitted ellipse, respectively. If multiple DLMs are available for a particular galaxy cluster, the median ϵ is used. The distribution of ϵ (right panel of Figure 4) matches our expectation, with the complex and elongated structures of the HFF and RELICS galaxy clusters resulting in high values of ϵ. We find $\epsilon < 0.5$ values only in the CLASH and SGAS clusters.

Figure 5 shows the mass ratio between the efficient mass estimates and the DLM. Results from the mass enclosed by the Einstein radius method are shown in the left panels, and SHMs are shown in the right panels. In the top panels, we plot the mass ratios against the respective apertures within which they are measured, θ_{arcs} (left) and $e\theta_{E,SHM}$ (right). The galaxy cluster
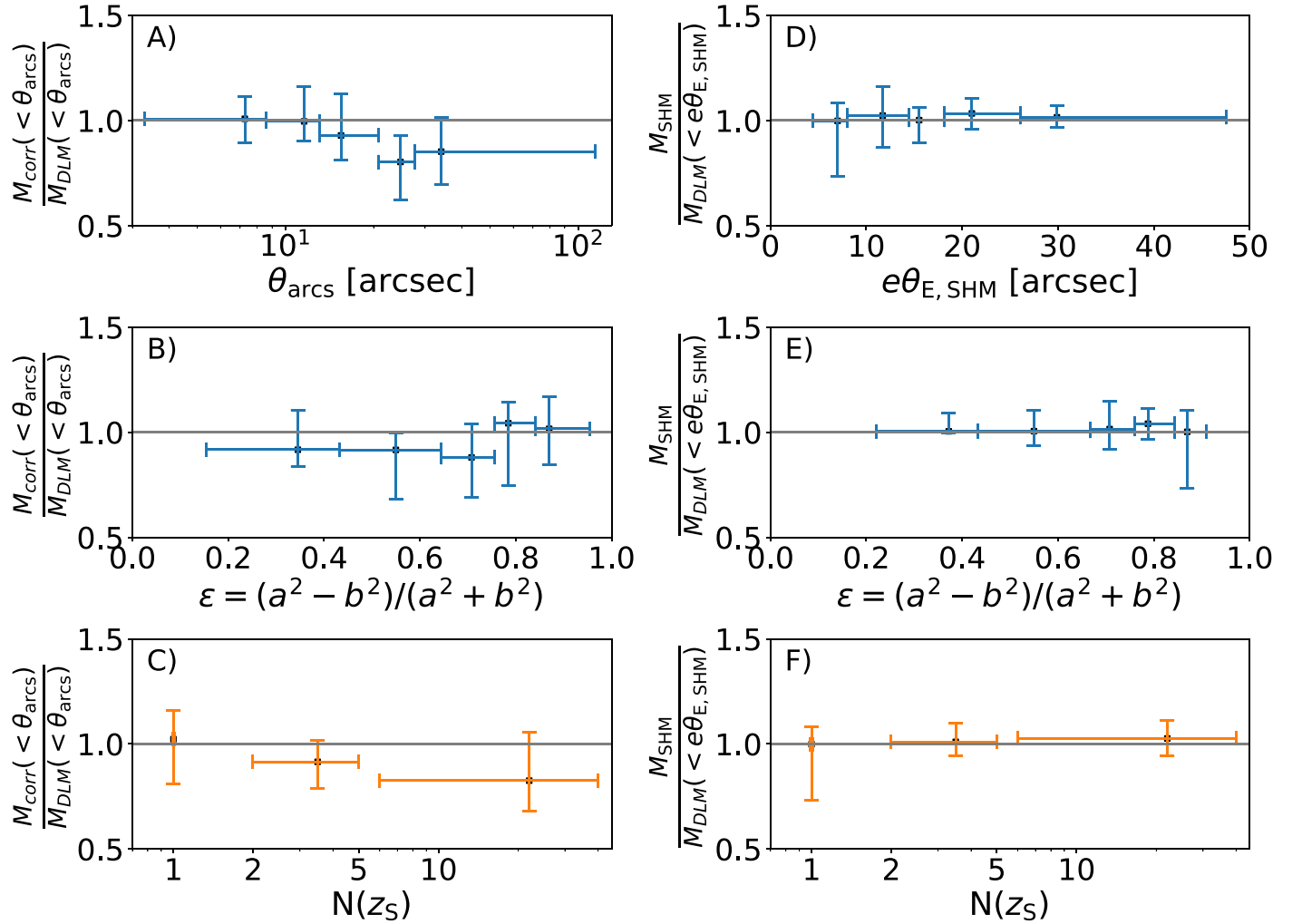
Figure 5. Mass ratio, $M_{corr}(<\theta_{arcs})/M_{DLM}(<\theta_{arcs})$ and $M_{SHM}/M_{DLM}(<e\theta_{E,SHM})$, binned by radii; deviation from circular symmetry; and number of background sources with spectroscopic redshift. Shown are the mass ratio between the efficient mass estimates and the mass from the DLMs, $M_{corr}(<\theta_{arcs})/M_{DLM}(<\theta_{arcs})$ (left panels) and $M_{SHM}/M_{DLM}(<e\theta_{E,SHM})$ (right panels), binned by the approximate Einstein radius (θ_{arcs}; panel A), the SHM aperture ($e\theta_{E,SHM}$; panel D), the total number of multiply imaged lensed background sources with spectroscopic redshifts ($N(z_S)$; panels B and E), and the deviation from circular symmetry (ϵ; panels C and F). The bins for θ_{arcs}, $e\theta_{E,SHM}$, and ϵ each have an equal number of points from the statistical samples of 67,000 and 54,000; see Section 4.4. The $N(z_S)$ is divided into three bins, $N(z_S) = 1$, $2 \leqslant N(z_S) \leqslant 5$, and $N(z_S) \geqslant 6$, and do not have the same number of points per bin. The symbols indicate the median of the distribution, and the error bars in the horizontal and vertical directions indicate the bin range and the scatter (the 16th and 84th percentiles), respectively. We observe an overall negative bias in $M_{corr}(<\theta_{arcs})$ in panels A, B, and C. We find a zero bias in the first two θ_{arcs} bins, where this method is well calibrated, and a negative bias at higher radii (panel A). The larger bias in the high-$N(z_S)$ bins reflects the difficulty of this single-component mass estimate to reconstruct the DLM complexity that is enabled by a large number of lensing constraints. In panels D, E, and F, we find that the mass ratio has little bias across all systematics we explore. We find a slight trend in the scatter in panels D and E, where the scatter decreases with increasing $e\theta_{E,SHM}$ (panel D) and decreasing ϵ (panel E).

deviation from circular symmetry, ϵ, is shown in the middle panels, and the number of multiply imaged lensed background sources with spectroscopic redshifts, $N(z_S)$, is shown in the bottom panels. In the radii and ellipticity panels, we use five bins with equal numbers of statistical sample points, 67,000 and 54,000 for $M_{corr}(<\theta_{arcs})$ and M_{SHM}, respectively. The $N(z_S)$ sample is divided into three nonuniform bins as described above. The symbols indicate the median of the distribution, and the error bars in the horizontal and vertical directions indicate the bin range and the scatter (the 16th and 84th percentiles), respectively.

In panel A of Figure 5, we find an indication of a decreasing trend in the mass ratio with increasing θ_{arcs}. The last bin of θ_{arcs} is just consistent with a mass ratio of 1.0, which we attribute to the change of the empirical correction from quadratic to linear for $\theta_{arcs} > 30\rlap{.}''0$ (see Section 3.3). We confirm that in the region where the empirical correction was calibrated, $\theta_{arcs} < 20\rlap{.}''0$,

there is no bias. The negative bias observed at large θ_{arcs} could possibly be addressed by extending the work of Remolina González et al. (2020) to larger clustercentric radii and lower magnification. In panel B, we identify that, while all ellipticity bins are consistent with a mass ratio of 1.0, the lower ϵ bins have a small negative bias, while the opposite is observed for large ϵ. The large number of galaxy clusters with large ellipticities that include many arcs with small θ_{arcs} may explain the trends seen in panels A and B. Finally, in panel C, we find that while all three bins are consistent with a mass ratio of 1.0, a trend of larger negative bias in the bins with higher $N(z_S)$ is identified. The highest bin highlights the HFF clusters and three CLASH clusters. The large number of constraints allows for highly flexible and complex DLMs. These galaxy clusters are also well known to have complex mass distributions that are not well represented by a circularly symmetric mass distribution. In addition, the extensive deep observations and follow-up

work have allowed identification of SL evidence at large clustercentric distances, explaining the negative bias.

We find that M_{SHM} (panels D, E, and F) has a very low bias, and no trend is identified between the bias and $e\theta_{E,SHM}$, ϵ, and $N(z_S)$. In panel D, we observe a trend of decreasing scatter with increasing aperture radius. In panel E, we also identify a trend of increasing scatter with increasing ϵ. This trend matches our expectations, as highly elongated and complex mass distributions represented by an elongated critical curve will have a larger uncertainty when applying the SHMs, as these models are less complex than DLMs.

5.4. Comparison to the Statistical Uncertainty of the DLMs

To contextualize the scatter of the mass estimates assessed in this paper, we review it against the uncertainty typically attributed to DLMs. We plot in Figure 6 the overall scatter in the $M_{corr}(<\theta_{arcs})$ and M_{SHM} measurements against the statistical uncertainty of the DLMs, M_{range}/M_{DLM}, derived from the ratio of the range maps and the best-fit DLM. The statistical uncertainty of the DLMs is computed in the same way as the scatter (see Section 5), except the uncertainty of each data point is drawn from the publicly available range maps provided by the lensing teams and represents a statistical sampling of the parameter space, typically using Markov Chain Monte Carlo. The aggregated statistical uncertainty over the entire sample from the DLMs is $\sigma(M_{DLM}) = 1.1\%$.

However, the statistical DLM modeling uncertainty is likely underestimated. Comparing models of two simulated clusters that were computed by different DLM algorithms, Meneghetti et al. (2017) concluded that DLMs are reliable when recovering the enclosed mass in the inner $100\overset{''}{.}0$ with a scatter of less than 10%. In a recent comparison between DLM algorithms, Raney et al. (2020b) showed that while the mass measured by the DLMs is reliable, the statistical uncertainty reported by the lensing algorithms underestimates the systematic uncertainty. Raney et al. (2020b) estimated the systematic uncertainty at ∼5% for a circularly averaged mass computed from the most recent version (v4) of the HFF lens models.

5.5. Comparison between Observations and Simulations

Remolina González et al. (2020, 2021) measured the scatter and bias of $M_{corr}(<\theta_{arcs})$ and M_{SHM} against the "true" mass from simulations. To compare the scatter found in this work to Remolina González et al. (2020, 2021), we need to account for the fact that DLMs are an observable measurement and, while reliable, are not the absolute truth. The expected scatter should therefore be a combination of the intrinsic scatter of the mass estimate, as measured from simulations, and the scatter attributed to the DLM measurement.

We note that the scatter between the three mass estimates ($M_{corr}(<\theta_{arcs})$, M_{SHM}, and M_{DLM}) may be correlated. To fully characterize the correlations between the masses will require the computation of DLMs for a large sample of simulated SL galaxy clusters, which awaits new large cosmological simulations with baryonic information and will require an extensive amount of computational and human resources.

With this in mind, we compute a lower limit in the expected scatter by assuming that the scatter between the masses is uncorrelated. We add in quadrature the scatter of $M_{corr}(<\theta_{arcs})$ and M_{SHM} from simulations (10.9% and 3.3%, respectively, from Remolina González et al. 2020, 2021) with a 5% scatter in
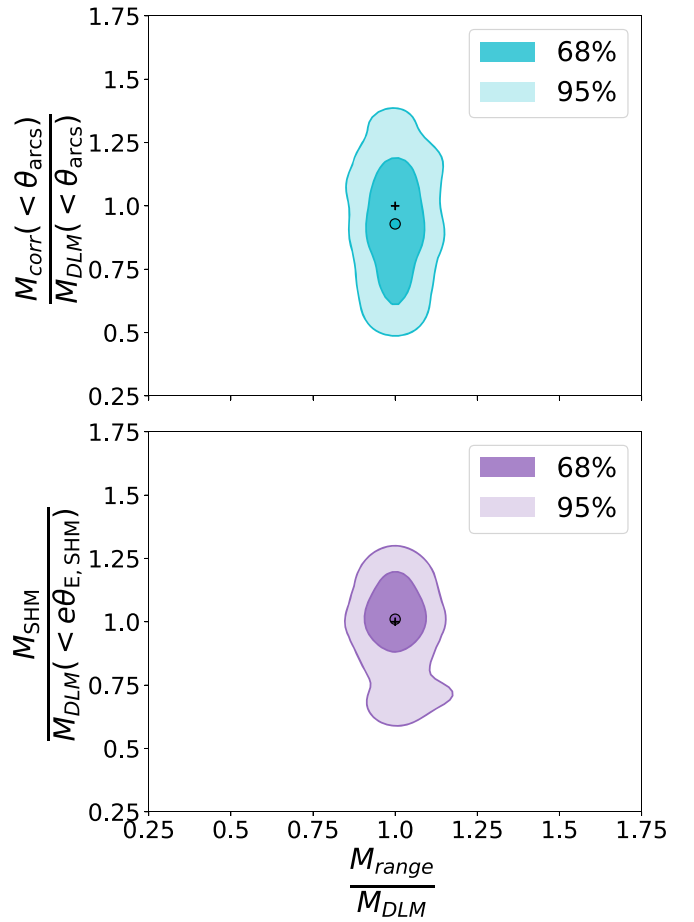

Figure 6. Scatter of the efficient mass estimate methods compared to the statistical uncertainty of the DLMs. We plot the mass ratio between the mass estimate and the best-fit DLM against the statistical scatter of the DLMs, M_{range}/M_{DLM}, derived from the ratio of publicly available range maps and best-fit DLMs. The plus signs stand for the point (1.0, 1.0), and the open circles indicate the median of the distributions. Results are shown for $M_{corr}(<\theta_{arcs})$ in the top panel and M_{SHM} in the bottom panel, smoothed by a kernel of 5%. The black plus sign indicates the location where $M_{corr}(<\theta_{arcs})$ and M_{SHM} equal M_{DLM}.

M_{DLM} (from Raney et al. 2020b). This results in an expected scatter of 12.0% for $M_{corr}(<\theta_{arcs})$ and 6.0% for M_{SHM} that passed the visual inspection. In both cases, we find that the overall scatter measured in this work (18.1% and 8.2%) is larger than expected. The difference between these scatters highlights some of the limitations in the simulation used by Remolina González et al. (2020, 2021) to account for the full range of scatter due to, e.g., baryonic effects, uncorrelated mass along the line of sight, and shear from nearby structures.

6. Summary and Conclusions

A large number of SL galaxy clusters is expected to be detected in current and upcoming large surveys. Estimating the mass at the core of these galaxy clusters will serve as one of the anchors to the radial mass distribution profile and measurement of the concentration. The DLMs to analyze these SL clusters and measure the mass at the core of the galaxy cluster are limited by the small number of constraints available from the identified multiply imaged lensed sources, and each can take multiple weeks to be finalized. Timely, efficient, and accurate methods to measure the mass at the cores of galaxy clusters in these large samples are needed. Remolina González et al. (2020) assessed

an empirically corrected mass $M_{corr}(<\theta_{arcs})$ enclosed by the lensing evidence by assuming that their radial extent approximates the Einstein radius and using the Einstein radius equation for a spherically symmetric lens. Remolina González et al. (2021) assessed an aperture mass computed from SHMs, M_{SHM}. Both papers utilized simulated SL images from the Outer Rim (Heitmann et al. 2019). In this work, we apply the two methods to observational data and use the publicly available DLMs from the SGAS, CLASH, HFF, and RELICS SL cluster samples to evaluate the efficacy of the methods in measuring the core mass of galaxy clusters. We conclude the following.

1. The corrected mass enclosed by the approximate Einstein radius, $M_{corr}(<\theta_{arcs})$, has an overall scatter of 18.1% and bias of -7.1% compared to the DLMs. The bias is reduced if large radii ($\theta_{arcs} > 20\rlap{.}{''}0$) are excluded. For $\theta_{arcs} \leqslant 20\rlap{.}{''}0$, the scatter is 14.4%, and the bias is -4.3%.

2. The SHM aperture mass, when computed over the entire sample, has an overall scatter of 12.4% and bias of 2.4% compared to the DLM. A quick visual inspection of the SHM outputs eliminates the SHMs that fail to reproduce the lensing configuration, reducing the scatter to 8.2% and the bias to 1.0%. We find that the quick visual inspection is beneficial in reducing the scatter and bias between M_{SHM} and M_{DLM} and identify lines of sight that would benefit from a more detailed analysis.

3. We confirm that in the region where the empirical correction was calibrated, $\theta_{arcs} < 20\rlap{.}{''}0$, there is nearly no bias in $M_{corr}(<\theta_{arcs})$. We find that the bias in $M_{corr}(<\theta_{arcs})$ increases toward higher θ_{arcs} (see Figure 5). This trend could possibly be addressed by extending the work of Remolina González et al. (2020) to larger clustercentric radii and lower magnification.

4. We explore the bias and scatter of M_{SHM} and find a small positive bias and no trend with respect to the SHM-derived effective Einstein radius, $e\theta_{E,SHM}$; the deviation from circular symmetry; or the number of multiply imaged background sources with spectroscopic redshifts (see Figure 5). We find a slight trend in the scatter of M_{SHM} in panels D and E, where the scatter decreases with increasing $e\theta_{E,SHM}$ (panel D) and decreasing ϵ (panel E).

5. To compare the overall scatter from $M_{corr}(<\theta_{arcs})$ and M_{SHM} to that of simulations, we need to take into account the uncertainty in the DLMs. While we expect correlations between all mass estimates ($M_{corr}(<\theta_{arcs})$, M_{SHM}, and M_{DLM}), computing this is outside the scope of this analysis. We choose to compute a lower limit for the expected scatter by adding in quadrature 5%, which corresponds to the scatter of the mass from the DLMs, to the scatter measured in the simulation of 10.9% for $M_{corr}(<\theta_{arcs})$ and 3.3% for M_{SHM} that passed the visual inspection. The resulting expected scatter is 12.0% for the corrected mass enclosed by the approximate Einstein radius and 6.0% for the SHMs that passed the visual inspection. The measured scatter in this work for both cases, 18.1% in $M_{corr}(<\theta_{arcs})$ and 8.2% in M_{SHM}, is higher than our estimated lower limit of the expected scatter. The difference is attributed to limitations in the simulation used by Remolina González et al. (2020, 2021), including baryonic effects, line-of-sight structure, and shear due to nearby structures.

6. The DLMs are considered to be the state of the art in measuring the enclosed projected mass density within the cores of galaxy clusters. While likely underestimated, the relative statistical lens modeling uncertainty of DLMs, marginalized over the large sample we investigated here, is of order 1.1%. Systematic uncertainties are estimated in the literature (e.g., Meneghetti et al. 2017; Raney et al. 2020b) at the 5%–10% level. We show that the precision toll of using the significantly faster mass estimate methods is only an 8.2% or 18.1% increase over the DLMs. We conclude that if other, larger, sources of error dominate the analysis, these fast and efficient mass estimate methods become a powerful tool in analyses of large cluster samples.

Overall, this work demonstrates the successful application of these efficient methods to observational data as currently established, as well as their reliability in estimating the mass at the core of strong gravitational lensing galaxy clusters. We look forward to improvements to these methods benefiting from identification of SL evidence by convolutional neural networks (e.g., Canameras et al. 2020; Huang et al. 2021; Morgan et al. 2021) and other machine-learning algorithms to model the mass distribution of the SL clusters (e.g., Bom et al. 2019; Pearson et al. 2019).

ORCID iDs

J. D. Remolina González https://orcid.org/0000-0002-7868-9827
K. Sharon https://orcid.org/0000-0002-7559-0864
G. Mahler https://orcid.org/0000-0003-3266-2001
C. Fox https://orcid.org/0000-0001-8316-9482
K. Napier https://orcid.org/0000-0003-4470-1696
L. E. Bleem https://orcid.org/0000-0001-7665-5079
M. D. Gladders https://orcid.org/0000-0003-1370-5010
N. Li https://orcid.org/0000-0001-6800-7389
A. Niemiec https://orcid.org/0000-0003-3791-2647

References

Acebron, A., Alon, M., Zitrin, A., et al. 2019, ApJ, 874, 132
Acebron, A., Cibirka, N., Zitrin, A., et al. 2018, ApJ, 858, 42
Acebron, A., Jullo, E., Limousin, M., et al. 2017, MNRAS, 470, 1809
Acebron, A., Zitrin, A., Coe, D., et al. 2020, ApJ, 898, 6
Abazajian, K. N., Adelman-McCarthy, J. K., Agüeros, M. A., et al. 2009, ApJS, 182, 543
Allen, S. W., Evrard, A. E., & Mantz, A. B. 2011, ARA&A, 49, 409
Bartelmann, M. 2010, CQGra, 27, 233001
Bayliss, M. B. 2012, ApJ, 744, 156

Bayliss, M. B., Gladders, M. D., Oguri, M., et al. 2011a, ApJL, 727, L26
Bayliss, M. B., Hennawi, J. F., Gladders, M. D., et al. 2011b, ApJS, 193, 8
Bayliss, M. B., Johnson, T., Gladders, M. D., Sharon, K., & Oguri, M. 2014, ApJ, 783, 41
Bayliss, M. B., Wuyts, E., Sharon, K., et al. 2010, ApJ, 720, 1559
Benson, B. A., Ade, P. A. R., Ahmed, Z., et al. 2014, Proc. SPIE, 9153, 91531P
Blanton, M. R., Bershady, M. A., Abolfathi, B., et al. 2017, AJ, 154, 28
Bleem, L. E., Stalder, B., de Haan, T., et al. 2015, ApJS, 216, 27
Bocquet, S., Dietrich, J. P., Schrabback, T., et al. 2019, ApJ, 878, 55
Bocquet, S., Heitmann, K., Habib, S., et al. 2020, ApJ, 901, 5
Bom, C., Poh, J., Nord, B., Blanco-Valentin, M., & Dias, L. 2019, arXiv:1911.06341
Bradač, M., Clowe, D., Gonzalez, A. H., et al. 2006, ApJ, 652, 937
Bradač, M., Schrabback, T., Erben, T., et al. 2008, ApJ, 681, 187
Bradač, M., Treu, T., Applegate, D., et al. 2009, ApJ, 706, 1201
Broadhurst, T., Benítez, N., Coe, D., et al. 2005, ApJ, 621, 53
Broadhurst, T. J., & Barkana, R. 2008, MNRAS, 390, 1647
Caminha, G. B., Grillo, C., Rosati, P., et al. 2017, A&A, 600, A90
Caminha, G. B., Rosati, P., Grillo, C., et al. 2019, A&A, 632, A36
Canameras, R., Schuldt, S., Suyu, S. H., et al. 2020, A&A, 644, A163
Cerny, C., Sharon, K., Andrade-Santos, F., et al. 2018, ApJ, 859, 159
Child, H. L., Habib, S., Heitmann, K., et al. 2018, ApJ, 859, 55
Cibirka, N., Acebron, A., Zitrin, A., et al. 2018, ApJ, 863, 145
Coe, D., Salmon, B., Bradač, M., et al. 2019, ApJ, 884, 85
Coe, D., Zitrin, A., Carrasco, M., et al. 2013, ApJ, 762, 32
Diego, J. M., Broadhurst, T., Wong, J., et al. 2016, MNRAS, 459, 3447
Diego, J. M., Protopapas, P., Sandvik, H. B., & Tegmark, M. 2005, MNRAS, 360, 477
Diego, J. M., Tegmark, M., Protopapas, P., & Sandvik, H. B. 2007, MNRAS, 375, 958
Diehl, H. T., Allam, S. S., Annis, J., et al. 2009, ApJ, 707, 686
Duffy, A. R., Schaye, J., Kay, S. T., & Dalla Vecchia, C. 2008, MNRAS, 390, L64
Ebeling, H., Ma, C. J., Kneib, J. P., et al. 2009, MNRAS, 395, 1213
Ebeling, H., Qi, J., & Richard, J. 2017, MNRAS, 471, 3305
Elíasdóttir, Á., Limousin, M., Richard, J., et al. 2007, arXiv:0710.5636
Evrard, A. E., MacFarland, T. J., Couchman, H. M. P., et al. 2002, ApJ, 573, 7
Fitzgibbon, A. W., Pilu, M., & Fisher, R. B. 1996, in Proc. 13th Int. Conf. on Pattern Recognition (Piscataway, NJ: IEEE), 253
Fox, C., Mahler, G., Sharon, K., & Remolina González, J. D. 2021, arXiv:2104.05585
Gladders, M. D., & Yee, H. K. C. 2000, AJ, 120, 2148
Gonzalez, A. H., Stanford, S. A., Brodwin, M., et al. 2012, ApJ, 753, 163
Gralla, M. B., Sharon, K., Gladders, M. D., et al. 2011, ApJ, 737, 74
Graur, O., Rodney, S. A., Maoz, D., et al. 2014, ApJ, 783, 28
Halkola, A., Hildebrandt, H., Schrabback, T., et al. 2008, A&A, 481, 65
Heitmann, K., Finkel, H., Pope, A., et al. 2019, ApJS, 245, 16
Hennawi, J. F., Gladders, M. D., Oguri, M., et al. 2008, AJ, 135, 664
Hsu, L.-Y., Ebeling, H., & Richard, J. 2013, MNRAS, 429, 833
Huang, K.-H., Lemaux, B. C., Schmidt, K. B., et al. 2016, ApJL, 823, L14
Huang, X., Storfer, C., Gu, A., et al. 2021, ApJ, 909, 27
Huterer, D., & Shafer, D. L. 2018, RPPh, 81, 016901
Ishigaki, M., Kawamata, R., Ouchi, M., et al. 2015, ApJ, 799, 12
Jauzac, M., Richard, J., Jullo, E., et al. 2015, MNRAS, 452, 1437
Jauzac, M., Richard, J., Limousin, M., et al. 2016, MNRAS, 457, 2029
Johnson, T. L., & Sharon, K. 2016, ApJ, 832, 82
Johnson, T. L., Sharon, K., Bayliss, M. B., et al. 2014, ApJ, 797, 48
Johnson, T. L., Sharon, K., Gladders, M. D., et al. 2017, ApJ, 843, 78
Jullo, E., & Kneib, J. P. 2009, MNRAS, 395, 1319
Jullo, E., Kneib, J. P., Limousin, M., et al. 2007, NJPh, 9, 447
Karman, W., Caputi, K. I., Caminha, G. B., et al. 2017, A&A, 599, A28
Kawamata, R., Ishigaki, M., Shimasaku, K., et al. 2018, ApJ, 855, 4
Kawamata, R., Oguri, M., Ishigaki, M., Shimasaku, K., & Ouchi, M. 2016, ApJ, 819, 114
Keeton, C. R. 2010, GReGr, 42, 2151
Khedekar, S., & Majumdar, S. 2013, JCAP, 2013, 030
Killedar, M., Borgani, S., Fabjan, D., et al. 2018, MNRAS, 473, 1736
Kneib, J. P., Ellis, R. S., Smail, I., Couch, W. J., & Sharples, R. M. 1996, ApJ, 471, 643
Kneib, J.-P., & Natarajan, P. 2011, A&ARv, 19, 47
Kochanek, C. S. 2006, in Strong Gravitational Lensing, ed. G. Meylan et al. (Berlin: Springer), 91
Koester, B. P., Gladders, M. D., Hennawi, J. F., et al. 2010, ApJL, 723, L73
Kubo, J. M., Allam, S. S., Drabek, E., et al. 2010, ApJL, 724, L137
Lagattuta, D. J., Richard, J., Bauer, F. E., et al. 2019, MNRAS, 485, 3738
Liesenborgs, J., De Rijcke, S., & Dejonghe, H. 2006, MNRAS, 367, 1209
Limousin, M., Ebeling, H., Ma, C. J., et al. 2010, MNRAS, 405, 777
Limousin, M., Richard, J., Jullo, E., et al. 2016, A&A, 588, A99
Lotz, J. M., Koekemoer, A., Coe, D., et al. 2017, ApJ, 837, 97
LSST Science Collaboration, Marshall, P., Anguita, T., et al. 2017, arXiv:1708.04058
Mahler, G., Richard, J., Clément, B., et al. 2018, MNRAS, 473, 663
Mahler, G., Sharon, K., Fox, C., et al. 2019, ApJ, 873, 96
Mainali, R., Stark, D. P., Tang, M., et al. 2020, MNRAS, 494, 719
Mantz, A. B., Allen, S. W., Morris, R. G., et al. 2014, MNRAS, 440, 2077
McCully, C., Keeton, C. R., Wong, K. C., & Zabludoff, A. I. 2014, MNRAS, 443, 3631
Meneghetti, M., Bartelmann, M., Dahle, H., & Limousin, M. 2013, SSRv, 177, 31
Meneghetti, M., Natarajan, P., Coe, D., et al. 2017, MNRAS, 472, 3177
Meneghetti, M., Rasia, E., Merten, J., et al. 2010, A&A, 514, A93
Meneghetti, M., Rasia, E., Vega, J., et al. 2014, ApJ, 797, 34
Merten, J., Meneghetti, M., Postman, M., et al. 2015, ApJ, 806, 4
Mohammed, I., Liesenborgs, J., Saha, P., & Williams, L. L. R. 2014, MNRAS, 439, 2651
Morgan, R., Nord, B., Birrer, S., Lin, J., & Poh, J. 2021, JOSS, 6, 2854
Narayan, R., & Bartelmann, M. 1996, arXiv:astro-ph/9606001
Newman, A. B., Treu, T., Ellis, R. S., & Sand, D. J. 2011, ApJL, 728, L39
Newman, A. B., Treu, T., Ellis, R. S., et al. 2013, ApJ, 765, 24
Niemiec, A., Jauzac, M., Jullo, E., et al. 2020, MNRAS, 493, 3331
Ofek, E. O., Seitz, S., & Klein, F. 2008, MNRAS, 389, 311
Oguri, M. 2010, PASJ, 62, 1017
Oguri, M., Bayliss, M. B., Dahle, H., et al. 2012, MNRAS, 420, 3213
Paterno-Mahler, R., Sharon, K., Coe, D., et al. 2018, ApJ, 863, 154
Pearson, J., Li, N., & Dye, S. 2019, MNRAS, 488, 991
Pillepich, A., Reiprich, T. H., Porciani, C., Borm, K., & Merloni, A. 2018, MNRAS, 481, 613
Planck Collaboration, Ade, P. A. R., Aghanim, N., et al. 2016, A&A, 594, A27
Postman, M., Coe, D., Benítez, N., et al. 2012, ApJS, 199, 25
Pratt, G. W., Arnaud, M., Biviano, A., et al. 2019, SSRv, 215, 25
Priewe, J., Williams, L. L. R., Liesenborgs, J., Coe, D., & Rodney, S. A. 2017, MNRAS, 465, 1030
Raney, C. A., Keeton, C. R., & Brennan, S. 2020a, MNRAS, 492, 503
Raney, C. A., Keeton, C. R., Brennan, S., & Fan, H. 2020b, MNRAS, 494, 4771
Ravindranath, S., & Ho, L. C. 2002, ApJ, 577, 133
Remolina González, J. D., Sharon, K., Li, N., et al. 2021, ApJ, 910, 146
Remolina González, J. D., Sharon, K., & Mahler, G. 2018, ApJ, 863, 60
Remolina González, J. D., Sharon, K., Reed, B., et al. 2020, ApJ, 902, 44
Richard, J., Claeyssens, A., Lagattuta, D. J., et al. 2021, A&A, 646, A83
Richard, J., Kneib, J.-P., Ebeling, H., et al. 2011, MNRAS, 414, L31
Rigby, J. R., Bayliss, M. B., Sharon, K., et al. 2018, AJ, 155, 104
Salmon, B., Coe, D., Bradley, L., et al. 2018, ApJL, 864, L22
Salmon, B., Coe, D., Bradley, L., et al. 2020, ApJ, 889, 189
Schneider, P. 2006, in Introduction to Gravitational Lensing and Cosmology, ed. G. Meylan (Berlin Heidelberg: Springer), 1
Sebesta, K., Williams, L. L. R., Liesenborgs, J., Medezinski, E., & Okabe, N. 2019, MNRAS, 488, 3251
Sharon, K., Bayliss, M. B., Dahle, H., et al. 2017, ApJ, 835, 5
Sharon, K., Bayliss, M. B., Dahle, H., et al. 2020, ApJS, 247, 12
Sharon, K., Gladders, M. D., Rigby, J. R., et al. 2012, ApJ, 746, 161
Shin, T., Adhikari, S., Baxter, E. J., et al. 2019, MNRAS, 487, 2900
Smith, G. P., Kneib, J.-P., Ebeling, H., Czoske, O., & Smail, I. 2001, ApJ, 552, 493
Smith, G. P., Kneib, J.-P., Smail, I., et al. 2005, MNRAS, 359, 417
Stark, D. P., Auger, M., Belokurov, V., et al. 2013, MNRAS, 436, 1040
Strait, V., Bradač, M., Coe, D., et al. 2020, ApJ, 888, 124
Strait, V., Bradač, M., Hoag, A., et al. 2018, ApJ, 868, 129
Sunyaev, R. A., & Zeldovich, Y. B. 1970, Ap&SS, 7, 3
Umetsu, K., & Diemer, B. 2017, ApJ, 836, 231
Vega-Ferrero, J., Diego, J. M., & Bernstein, G. M. 2019, MNRAS, 486, 5414
Zitrin, A., Broadhurst, T., Umetsu, K., et al. 2009, MNRAS, 396, 1985
Zitrin, A., Fabris, A., Merten, J., et al. 2015, ApJ, 801, 44
Zitrin, A., Rosati, P., Nonino, M., et al. 2012, ApJ, 749, 97
Zitrin, A., Zheng, W., Broadhurst, T., et al. 2014, ApJL, 793, L12